AIAA Meeting Papers on Disc, January 1997
A9715741, F49620-94-1-0019, F49620-95-1-0405, AIAA Paper 97-0726

An efficient semi-implicit time accurate scheme for unsteady viscous flow on dynamic grids

Xiaolin Zhong
California Univ., Los Angeles

Jian W. Shen
California Univ., Los Angeles

AIAA, Aerospace Sciences Meeting & Exhibit, 35th, Reno, NV, Jan. 6-9, 1997

This paper presents a semi-implicit method for efficient and high-order time-accurate computations for unsteady viscous hypersonic flows over fixed or moving bodies using Navier-Stokes equations. The equations are discretized in space using a second-order TVD scheme on moving structured grids. If explicit schemes are used to advance the equations in time, the small grid sizes in the wall-normal direction in the boundary layers imposed severe restrictions on the time steps. In the current method, the spatial discretization of the governing equations is separated into stiff terms involving derivatives along the wall-normal direction and nonstiff terms for the rest of the equations. The split equations are then advanced in time using second- and third-order semi-implicit Runge-Kutta schemes so that the nonstiff streamwise terms are treated by explicit Runge-Kutta methods and stiff wall-normal terms are simultaneously treated by implicit Runge-Kutta methods. The semi-implicit method leads to block pentagonal diagonal systems of implicit equations that can be solved efficiently. (Author)

An Efficient Semi-Implicit Time Accurate Scheme for Unsteady Viscous Flow on Dynamic Grids

Xiaolin Zhong * and Jian Wei Shen †
University of California, Los Angeles, California 90095

Abstract

This paper presents a semi-implicit method for efficient and high-order time-accurate computations for unsteady viscous hypersonic flows over fixed or moving bodies using Navier-Stokes equations. The equations are discretized in space using a second-order TVD scheme on moving structured grids. If explicit schemes are used to advance the equations in time, the small grid sizes in wall-normal direction in the boundary layers imposed severe restriction on the time steps. In the current method, the spatial discretization of the governing equations is separated into stiff terms involving derivatives along the wall-normal direction and non-stiff terms of the rest of the equations. The split equations are then advanced in time using second and third-order semi-implicit Runge-Kutta schemes so that the non-stiff streamwise terms are treated by explicit Runge-Kutta methods and stiff wall-normal terms are simultaneously treated by implicit Runge-Kutta methods. The semi-implicit method leads to block pentagonal diagonal systems of implicit equations that can be solved efficiently. The strict limitation on time steps due to fine grids in the wall-normal direction is removed by semi-implicit method so that the time steps only depend on the grid spacing in the streamwise direction and accuracy requirement. The new semi-implicit algorithm is tested in computing the Navier-Stokes equations for unsteady hypersonic flows over an oscillating blunt body.

Introduction

Time accurate simulation of unsteady hypersonic flow with relative body motion is one of the great challenges to computational fluid dynamics. Recently, unstructured grid approach has been applied to solve the Euler equations[1, 2, 3, 4, 5, 6] and Navier-Stokes equations[7, 8, 9, 10, 11, 12, 13]. The advantage of unstructured grid methods is that they are flexible in handling complex geometries and in implementing solution adaptation. The disadvantage is that they are less efficient for viscous flow computations in the boundary layers where stretched girds with extremely small wall-normal grid sizes are required in order to capture unsteady flow scales. Since structured grids are much more efficient for such viscous flow computations, structured/unstructured hybrid grid approach has been used for numerical simulation of viscous flows[14, 15, 16] in which the boundary layers are solved using structured grids and the outer flow fields are solved using unstructured grids. For the computations of such unsteady viscous hypersonic flows with moving grids, as well as other transient hypersonic flow simulation with fixed grids, efficient and high-order accurate solvers are required.

For time-accurate hypersonic inviscid flow calculations, explicit methods are often used to solved the Euler equations because the time step sizes limited by the temporal accuracy requirements for unsteady flows are often comparable to the numerical stability conditions. For unsteady viscous flow calculations, however, the extremely small grid sizes in the boundary layers near the wall is used, the time steps required by the stability condition are much smaller than that needed by accuracy consideration. Consequently, the explicit computations of unsteady viscous flows are often not efficient enough for practical applications. In order to remove the severe stability restriction, global implicit methods have been used to treat the whole flow fields implicitly by approximate factorization methods or by iterative methods. For unsteady viscous flow computations, the full implicit treatment of global implicit methods is often unnecessary and inefficient because the time step is limited by the unsteady flow time scales and the streamwise terms in the equations can be treated by more efficient explicit methods.

In this paper, we present a high-order and efficient semi-implicit method to compute unsteady viscous hypersonic flows with fixed or moving structured grids. The new method is motivated by our long-

*Assistant Professor, Mechanical and Aerospace Engineering Department, Member AIAA.
†Research Associate, Mechanical and Aerospace Engineering Department, Member AIAA

term research project in direct numerical simulation of laminar-turbulent transition of hypersonic boundary layers[17] over fixed or maneuvering hypersonic vehicles. The Navier-Stokes equations for unsteady flows are discretized in space using a second-order TVD scheme, which can be replaced by other high-order schemes if necessary. The spatial discretization of the governing equations is separated into stiff terms involving derivatives along the wall-normal direction and the non-stiff terms of the rest of the equations. The split equations are advanced in time using second and third-order semi-implicit Runge-Kutta schemes recently derived by Zhong and Shen[18, 19]. The semi-implicit schemes lead to block pentagonal diagonal systems of implicit equations that can be solved efficiently. Meanwhile, the restriction on the time step is only limited by the streamwise grid sizes and by accuracy conditions.

Governing Equations

The two-dimensional Navier-Stokes equations in the integral form on moving meshes can be written as

$$\frac{\partial}{\partial t}\int\int_{\mathcal{V}} U d\mathcal{V} + \int_{\partial\mathcal{V}} \mathbf{E}\cdot d\mathbf{S} = 0 \tag{1}$$

where $d\mathbf{S}$ is surface outward pointing vector,

$$d\mathbf{S} = (n_x\mathbf{i} + n_y\mathbf{j})dS \tag{2}$$

U is the vector of the conservative variables, and $\mathbf{E}$ is the flux vector,

$$U = \begin{bmatrix} \rho \\ \rho u \\ \rho v \\ \rho e \end{bmatrix} \tag{3}$$

$$\mathbf{E} = (F - F_v)\,\mathbf{i} + (G - G_v)\,\mathbf{j} \tag{4}$$

where

$$F = \begin{bmatrix} \rho\,(u - x_t) \\ \rho u\,(u - x_t) + p \\ \rho v\,(u - x_t) \\ (\rho e + p)\,(u - x_t) + p x_t \end{bmatrix} \tag{5}$$

$$G = \begin{bmatrix} \rho\,(v - y_t) \\ \rho u\,(v - y_t) \\ \rho v\,(v - y_t) + p \\ (\rho e + p)\,(v - y_t) + p y_t \end{bmatrix} \tag{6}$$

$$F_v = \begin{bmatrix} 0 \\ \tau_{xx} \\ \tau_{xy} \\ u\tau_{xx} + v\tau_{xy} - q_x \end{bmatrix} \quad G_v = \begin{bmatrix} 0 \\ \tau_{yx} \\ \tau_{yy} \\ u\tau_{yx} + v\tau_{yy} - q_y \end{bmatrix} \tag{7}$$

where ρ is the fluid density, u and v are the x and y components of the fluid velocity. x_t and y_t are the grid speeds in the x and y directions, respectively. e is the total energy and p is the pressure.

$$e = \frac{p}{\rho(\gamma - 1)} + \frac{1}{2}(u^2 + v^2) \tag{8}$$

$$p = \rho R T \tag{9}$$

where R is the univers gas constant and γ is specific heat ratio.

The viscous stress τ and heating rate q are

$$\tau_{xx} = \frac{2}{3}\mu(2\frac{\partial u}{\partial x} - \frac{\partial v}{\partial y}) \tag{10}$$

$$\tau_{yy} = \frac{2}{3}\mu(2\frac{\partial v}{\partial y} - \frac{\partial u}{\partial x}) \tag{11}$$

$$\tau_{xy} = \tau_{yx} = \mu(\frac{\partial u}{\partial y} + \frac{\partial v}{\partial x}) \tag{12}$$

$$q_x = -k\frac{\partial T}{\partial x} \tag{13}$$

$$q_y = -k\frac{\partial T}{\partial y} \tag{14}$$

where the viscosity coefficient μ is computed according to the Sutherland's law, and heat conductivity k is determined by assuming a constant Prandtl number, the value of which is set to be 0.72 for air.

The boundary conditions for computing viscous hypersonic flows of moving blunt bodies are as follows. The outer boundary conditions are fixed as the freestream conditions. No physical boundary conditions are required at the supersonic exit boundaries where the flow variables are determined by the upstream conditions. On the solid wall, no-slip and isothermal boundary conditions are used.

Numerical Method

In the current semi-implicit methods, the spatial discretization of the Navier-Stokes equations is first additively split into the stiff viscous terms involving spatial derivatives normal to the wall and the rest of the flux

terms, which leads to a system of ordinary differential equations in the form of

$$\mathbf{u}' = \mathbf{f}(t, \mathbf{u}) + \mathbf{g}(t, \mathbf{u}) \tag{15}$$

where $\mathbf{u}$ represents all of the unknown discretized flow variables in the flow field, $\mathbf{f}(t, \mathbf{u})$ represents the non-stiff terms, and $\mathbf{g}(t, \mathbf{u})$ represents the stiff terms. The split ordinary differential equations (15) is then integrated in time using semi-implicit Runge-Kutta schemes derived by Zhong and Shen[18, 19], where $\mathbf{f}$ is treated by explicit Runge-Kutta methods and $\mathbf{g}$ is simultaneously treated by implicit Runge-Kutta methods. The resulting semi-implicit methods for time-accurate computations of the Navier-Stokes equations are high-order accurate in both space and time, and they are much more efficient than the spatially full implicit schemes. The details of the method is presented in the following sections.

Spatial Discretization and Splitting

The governing equations are discretized in space using a cell-centered finite-volume method. For a cell denoted by ij, Eq.(1) is discretized as

$$\begin{aligned}\frac{\partial U_{ij}}{\partial t} &= -\frac{1}{V_{ij}}\left[(\mathbf{E}\cdot\mathbf{S})_{i+\frac{1}{2},j} - (\mathbf{E}\cdot\mathbf{S})_{i-\frac{1}{2},j}\right] \\ &\quad -\frac{1}{V_{ij}}\left[(\mathbf{E}\cdot\mathbf{S})_{i,j+\frac{1}{2}} - (\mathbf{E}\cdot\mathbf{S})_{i,j-\frac{1}{2}}\right]\end{aligned} \tag{16}$$

where V_{ij} is the cell volum and index $i \pm 1/2$ and $j \pm 1/2$ represent cell boundaries. In Eq. (16), the inviscid fluxes F and G in $\mathbf{E}$ term are approximated by a second-order TVD scheme, i.e.,

$$\begin{aligned}n_xF + n_yG &= \frac{1}{2}\left[n_xF(U^R) + n_yG(U^R)\right] \\ &+ \frac{1}{2}\left[n_xF(U^L) + n_yG(U^L)\right] \\ &- \frac{1}{2}\hat{\mathbf{T}}|n_x\hat{\mathbf{\Lambda}}_F + n_y\hat{\mathbf{\Lambda}}_G|\hat{\mathbf{T}}^{-1}(U^R - U^L)\end{aligned} \tag{17}$$

where

$$U^R = U_{i+1} - \frac{1}{2}\mathbf{T_{i+1}}\,\text{minmod}[\mathbf{T_{i+1}^{-1}}(\triangle_{i+1}U, \triangle_i U)] \tag{18}$$

$$U^L = U_i + \frac{1}{2}\mathbf{T_i}\text{minmod}[\mathbf{T_i^{-1}}(\triangle_i U, \triangle_{i-1}U)] \tag{19}$$

$$\triangle_i U = U_{i+1} - U_i \tag{20}$$

$$\text{minmod}(x, y) = \frac{sign(x) + sign(y)}{2}\min(|x|, |y|) \tag{21}$$

$$\mathbf{A} = \mathbf{T\Lambda T^{-1}} \tag{22}$$

where $|\hat{\mathbf{A}}| = |\frac{\partial(n_xF+n_yG)}{\partial U}|$ is evaluated using Roe averages[20] at the surface. Meanwhile, the viscous flux parts in $\mathbf{E}$ term are approximated by central difference schemes.

The right hand side of Eq. (16) is additively split into relatively non-stiff term f_{ij} and stiff term g_{ij} as follows

$$\frac{\partial U_{ij}}{\partial t} = f_{ij} + g_{ij} \tag{23}$$

where

$$\begin{aligned}f_{ij} &= -\frac{1}{V_{ij}}[(\mathbf{E}\cdot\mathbf{S})_{i+\frac{1}{2},j} - (\mathbf{E}\cdot\mathbf{S})_{i-\frac{1}{2},j}] \\ &\quad +\frac{1}{V_{ij}}\left[(SE_{v1})_{i,j+\frac{1}{2}} - (SE_{v1})_{i,j-\frac{1}{2}}\right]\end{aligned} \tag{24}$$

$$\begin{aligned}g_{ij} &= -\frac{1}{V_{ij}}\{[S(n_xF + n_yG)]_{i,j+\frac{1}{2}} \\ &\quad -[S(n_xF + n_yG)]_{i,j-\frac{1}{2}}\} \\ &\quad + \frac{1}{V_{ij}}\left[(SE_{v2})_{i,j+\frac{1}{2}} - (SE_{v2})_{i,j-\frac{1}{2}}\right]\end{aligned} \tag{25}$$

where E_{v1} is the part of the viscous flux terms on the $j \pm 1/2$ surfaces involving tangential derivatives only, and E_{v2} is the part of the viscous flux terms on the $j \pm 1/2$ surfaces involving normal derivatives, i.e.,

$$n_xF_v + n_yG_v = E_{v1} + E_{v2} \tag{26}$$

and

$$E_{v1} = \begin{bmatrix} 0 \\ \tau_{\xi 2} \\ \tau_{\xi 3} \\ \tau_{\xi 4} \end{bmatrix} \qquad E_{v2} = \begin{bmatrix} 0 \\ \tau_{\eta 2} \\ \tau_{\eta 3} \\ \tau_{\eta 4} \end{bmatrix} \tag{27}$$

where

$$\begin{aligned}\tau_{\xi 2} &= \mu\left(\frac{4}{3}\xi_x n_x + \xi_y n_y\right)\frac{\partial u}{\partial \xi} \\ &\quad + \mu\left(-\frac{2}{3}\xi_y n_x + \xi_x n_y\right)\frac{\partial v}{\partial \xi}\end{aligned} \tag{28}$$

$$\tau_{\xi 3} = \mu\left(\xi_y n_x - \frac{2}{3}\xi_x n_y\right)\frac{\partial u}{\partial \xi} + \mu\left(\xi_x n_x + \frac{4}{3}\xi_y n_y\right)\frac{\partial v}{\partial \xi} \quad (29)$$

$$\tau_{\xi 4} = u\tau_{\xi 2} + v\tau_{\xi 3} + k\left(\xi_x n_x + \xi_y n_y\right)\frac{\partial T}{\partial \xi} \quad (30)$$

$$\tau_{\eta 2} = \mu\left(\frac{4}{3}\eta_x n_x + \eta_y n_y\right)\frac{\partial u}{\partial \eta} + \mu\left(-\frac{2}{3}\eta_y n_x + \eta_x n_y\right)\frac{\partial v}{\partial \eta} \quad (31)$$

$$\tau_{\eta 3} = \mu\left(\eta_y n_x - \frac{2}{3}\eta_x n_y\right)\frac{\partial u}{\partial \eta} + \mu\left(\eta_x n_x + \frac{4}{3}\eta_y n_y\right)\frac{\partial v}{\partial \eta} \quad (32)$$

$$\tau_{\eta 4} = u\tau_{\eta 2} + v\tau_{\eta 3} + k\left(\eta_x n_x + \eta_y n_y\right)\frac{\partial T}{\partial \eta} \quad (33)$$

Semi-Implicit RK Schemes

Applying the splitting of Eq. (23) to every grid cell of the flow field results in Eq. (15), which can be integrated in time using the second and third-order semi-implicit Runge-Kutta schemes[18, 19], where $\mathbf{f}$ is treated by explicit Runge-Kutta methods and $\mathbf{g}$ is simultaneously treated by implicit Runge-Kutta methods.

The second-order semi-implicit Runge-Kutta (ASIRK-2C) scheme is

$$[\mathbf{I} - ha_1\mathbf{J}(t^n, \mathbf{U}^n)]\,\mathbf{k_1} = h\,[\mathbf{f}(t^n, \mathbf{U}^n) + \mathbf{g}(t^n, \mathbf{U}^n)] \quad (34)$$

$$[\mathbf{I} - ha_2\mathbf{J}(t^n + s_2h, \mathbf{U}^n + c_{21}\mathbf{k_1})]\,\mathbf{k_2} = h\,[\mathbf{f}(t^n + r_2h, \mathbf{U}^n + b_{21}\mathbf{k_1}) + \mathbf{g}(t^n + s_2h, \mathbf{U}^n + c_{21}\mathbf{k_1})] \quad (35)$$

$$\mathbf{U}^{n+1} = \mathbf{U}^n + \omega_1\mathbf{k_1} + \omega_2\mathbf{k_2} \quad (36)$$

where

$\omega_1 = \frac{1}{2}$	$\omega_2 = \frac{1}{2}$	$a_1 = \frac{1}{4}$	$a_2 = \frac{1}{3}$
$b_{21} = 1$	$c_{21} = \frac{5}{12}$	$r_2 = 1$	$s_2 = 1$

The third-order semi-implicit Runge-Kutta (ASIRK-4C) scheme is[19]

$$\begin{cases} [\mathbf{I} - ha_1\mathbf{J}(t^n, U^n)]\,\mathbf{k}_1 = h\{\mathbf{f}(t^n, U^n) + \mathbf{g}(t^n, U^n)\} \\ [\mathbf{I} - ha_2\mathbf{J}(t^n + s_2h, U^n + c_{21}\mathbf{k}_1)]\,\mathbf{k}_2 = h\{\mathbf{f}(t^n + r_2h, \\ \quad U^n + b_{21}\mathbf{k}_1) + \mathbf{g}(t^n + s_2h, U^n + c_{21}\mathbf{k}_1)\} \\ [\mathbf{I} - ha_3\mathbf{J}(t^n + s_3h, U^n + c_{31}\mathbf{k}_1 + c_{32}\mathbf{k}_2)]\,\mathbf{k}_3 = h \\ \quad \{\mathbf{f}(t^n + r_3h, U^n + b_{31}\mathbf{k}_1 + b_{32}\mathbf{k}_2) \\ \quad +\mathbf{g}(t^n + s_3h, U^n + c_{31}\mathbf{k}_1 + c_{32}\mathbf{k}_2)\} \\ [\mathbf{I} - ha_4\mathbf{J}(t^n + s_4h, U^n + c_{41}\mathbf{k}_1 + c_{42}\mathbf{k}_2 + c_{42}\mathbf{k}_3)]\,\mathbf{k}_4 \\ \quad = h\{\mathbf{f}(t^n + r_4h, U^n + b_{41}\mathbf{k}_1 + b_{42}\mathbf{k}_2 + b_{43}\mathbf{k}_3) \\ \quad +\mathbf{g}(t^n + s_4h, U^n + c_{41}\mathbf{k}_1 + c_{42}\mathbf{k}_2 + c_{43}\mathbf{k}_3)\} \\ U^{n+1} = U^n + \omega_1\mathbf{k}_1 + \omega_2\mathbf{k}_2 + \omega_3\mathbf{k}_3 + \omega_4\mathbf{k}_4 \end{cases} \quad (37)$$

where

$\omega_1 = 0.125$	$\omega_2 = 0.25$	$\omega_3 = 0.525$
$\omega_4 = 0.1$	$b_{21} = 0.324692$	$b_{31} = 0.0877902$
$b_{32} = 0.671880$	$b_{41} = -0.2$	$b_{42} = -0.5$
$b_{43} = 0.9$	$a_1 = 0.283537$	$a_2 = 0.103555$
$a_3 = 0.115586$	$a_4 = 0.104866$	$c_{21} = 0.11$
$c_{31} = 0.0743829$	$c_{32} = 0.605617$	$c_{41} = 0.0759479$
$c_{42} = -0.586539$	$c_{43} = 0.340591$	

where r_i and s_i are given by $s_i = r_i = \sum_{j=1}^{i-1} b_{ij}$. The parameters with longer significant digits can be found in [19].

Jacobians for Semi-Implicit RK Schemes

In order to apply the semi-implicit Runge-Kutta schemes to the Navier-Stokes equations, Jacobian matrices are needed in the equations for $\mathbf{k_i}$. In order to maintain second and third-order temporal accuracy, the Jacobians need to be evaluated without any approximation. Especially, the derivative of the viscosity coefficient with respective to temperature needs to be included in the Jacobians. The details of Jacobian matrices, including the contributions from both inviscid fluxes and the viscous fluxes, are presented below.

Inviscid Flux Jacobian

The Jacobian for inviscid flux is

$$\delta(n_xF + n_yG) = \frac{1}{2}\left[\mathbf{M}(\mathbf{U^R}) - \hat{\mathbf{T}}|\hat{\mathbf{\Lambda}}|\hat{\mathbf{T}}^{-1}\right]\delta U^R + \frac{1}{2}\left[\mathbf{M}(\mathbf{U^L}) + \hat{\mathbf{T}}|\hat{\mathbf{\Lambda}}|\hat{\mathbf{T}}^{-1}\right]\delta U^L \quad (38)$$

where

$$\delta U^R = \delta U_{j+1} - \frac{1}{2}\alpha_1(\delta U_{j+2} - \delta U_{j+1})$$

$$-\frac{1}{2}\alpha_2(\delta U_{j+1}-\delta U_j) \quad (39)$$

$$\begin{aligned}\delta U^L &= \delta U_j+\frac{1}{2}\alpha_3(\delta U_{j+1}-\delta U_j)\\ &+ \frac{1}{2}\alpha_4(\delta U_j-\delta U_{j-1}) \quad (40)\end{aligned}$$

$$\mathbf{M}(\mathbf{U^R})=\left(n_x\frac{\partial F}{\partial U}+n_y\frac{\partial G}{\partial U}\right)_{U^R} \quad (41)$$

$$\mathbf{M}(\mathbf{U^L})=\left(n_x\frac{\partial F}{\partial U}+n_y\frac{\partial G}{\partial U}\right)_{U^L} \quad (42)$$

where $\alpha_\mathbf{k}, k=1,2,3,4$ are 4×4 diagonal matrices,

$$\alpha_\mathbf{k}=\begin{bmatrix}\alpha_{k1} & & & \\ & \alpha_{k2} & & \\ & & \alpha_{k3} & \\ & & & \alpha_{k4}\end{bmatrix} \quad (43)$$

when $(\mathbf{T^{-1}}_{j+1}\,\triangle_{j+1}\,U)_l\cdot(\mathbf{T^{-1}}_{j+1}\,\triangle_j\,U)_l>0$, $l=1,2,3,4$

$$\begin{cases}\alpha_{1l}=1\\ \alpha_{2l}=0\end{cases}\quad\text{if } |\mathbf{T^{-1}}_{j+1}(\triangle_{j+1}U)|_l<|\mathbf{T^{-1}}_{j+1}(\triangle_jU)|_l$$

$$\begin{cases}\alpha_{1l}=0\\ \alpha_{2l}=1\end{cases}\quad\text{if } |\mathbf{T^{-1}}_{j+1}(\triangle_{j+1}U)|_l\geq|\mathbf{T^{-1}}_{j+1}(\triangle_jU)|_l$$

when $(\mathbf{T^{-1}}_{j+1}\,\triangle_{j+1}\,U)_l\cdot(\mathbf{T^{-1}}_{j+1}\,\triangle_j\,U)_l\leq 0$, $l=1,2,3,4$

$$\begin{cases}\alpha_{1l}=0\\ \alpha_{2l}=0\end{cases}$$

when $(\mathbf{T^{-1}}_j\,\triangle_j\,U)_l\cdot(\mathbf{T^{-1}}_j\,\triangle_{j-1}\,U)_l>0$

$$\begin{cases}\alpha_{3l}=1\\ \alpha_{4l}=0\end{cases}\quad\text{if } |\mathbf{T^{-1}}_j(\triangle_jU)|_l<|\mathbf{T^{-1}}_j(\triangle_{j-1}U)|_l$$

$$\begin{cases}\alpha_{3l}=0\\ \alpha_{4l}=1\end{cases}\quad\text{if } |\mathbf{T^{-1}}_j(\triangle_jU)|_l\geq|\mathbf{T^{-1}}_j(\triangle_{j-1}U)|_l$$

when $(\mathbf{T^{-1}}_j\,\triangle_j\,U)_l\cdot(\mathbf{T^{-1}}_j\,\triangle_{j-1}\,U)_l\leq 0$

$$\begin{cases}\alpha_{3l}=0\\ \alpha_{4l}=0\end{cases}$$

Viscous Flux Jacobian

The Jacobian for viscous flux in the implicit parts is

$$\begin{aligned}\delta(E_{v2}) &= \mathbf{A_v}\,\delta V_{j+1}+\mathbf{B_v}\,\delta V_j\\ &= \mathbf{A_v}\frac{\partial V}{\partial U}\delta U_{j+1}+\mathbf{B_v}\frac{\partial V}{\partial U}\delta U_j \quad (44)\end{aligned}$$

where

$$V=\begin{bmatrix}\rho\\ u\\ v\\ T\end{bmatrix}\qquad \frac{\partial V}{\partial U}=\begin{bmatrix}0 & 0 & 0 & 0\\ -\frac{u}{\rho} & \frac{1}{\rho} & 0 & 0\\ -\frac{v}{\rho} & 0 & \frac{1}{\rho} & 0\\ 0 & 0 & 0 & \frac{\partial T}{\partial(\rho e)}\end{bmatrix} \quad (45)$$

$$\mathbf{A_v}=\begin{bmatrix}0 & 0 & 0 & 0\\ 0 & \frac{1}{\triangle\eta}a_{22} & \frac{1}{\triangle\eta}a_{23} & \frac{1}{2}\tau_{\eta 2}\frac{1}{\mu}\frac{d\mu}{dT}\\ 0 & \frac{1}{\triangle\eta}a_{32} & \frac{1}{\triangle\eta}a_{33} & \frac{1}{2}\tau_{\eta 3}\frac{1}{\mu}\frac{d\mu}{dT}\\ 0 & a_{42} & a_{43} & a_{44}\end{bmatrix} \quad (46)$$

$$\mathbf{B_v}=\begin{bmatrix}0 & 0 & 0 & 0\\ 0 & -\frac{1}{\triangle\eta}a_{22} & -\frac{1}{\triangle\eta}a_{23} & \frac{1}{2}\tau_{\eta 2}\frac{1}{\mu}\frac{d\mu}{dT}\\ 0 & -\frac{1}{\triangle\eta}a_{32} & -\frac{1}{\triangle\eta}a_{33} & \frac{1}{2}\tau_{\eta 3}\frac{1}{\mu}\frac{d\mu}{dT}\\ 0 & b_{42} & b_{43} & b_{44}\end{bmatrix} \quad (47)$$

and

$$a_{22}=\mu\left(\frac{4}{3}\eta_x n_x+\eta_y n_y\right) \quad (48)$$

$$a_{23}=\mu\left(-\frac{2}{3}\eta_y n_x+\eta_x n_x\right) \quad (49)$$

$$a_{32}=\mu\left(\eta_y n_x-\frac{2}{3}\eta_x n_y\right) \quad (50)$$

$$a_{33}=\mu\left(\eta_x n_x+\frac{3}{4}\eta_y n_y\right) \quad (51)$$

$$a_{42}=\frac{1}{\triangle\eta}u(a_{22}+a_{32})+\frac{1}{2}\tau_{\eta 2} \quad (52)$$

$$a_{43}=\frac{1}{\triangle\eta}v(a_{23}+a_{33})+\frac{1}{2}\tau_{\eta 3} \quad (53)$$

$$\begin{aligned}a_{44} &= \frac{1}{2}(u\tau_{\eta 2}+v\tau_{\eta 3})\frac{1}{\mu}\frac{d\mu}{dT}\\ &+ (\eta_x n_x+\eta_y n_y)[\frac{k}{\triangle\eta}+\frac{1}{2}\frac{\partial T}{\partial\eta}\frac{dk}{dT}] \quad (54)\end{aligned}$$

$$b_{42}=-\frac{1}{\triangle\eta}u(a_{22}+a_{32})+\frac{1}{2}\tau_{\eta 2} \quad (55)$$

$$b_{43}=-\frac{1}{\triangle\eta}v(a_{23}+a_{33})+\frac{1}{2}\tau_{\eta 3} \quad (56)$$

$$\begin{aligned}b_{44} &= \frac{1}{2}(u\tau_{\eta 2}+v\tau_{\eta 3})\frac{1}{\mu}\frac{d\mu}{dT}\\ &+ (\eta_x n_x+\eta_y n_y)[-\frac{k}{\triangle\eta}+\frac{1}{2}\frac{\partial T}{\partial\eta}\frac{dk}{dT}] \quad (57)\end{aligned}$$

Implicit Jacobian Matrix

The Jacobian matrix for the implicit parts of $(\mathbf{E}\cdot$

$\mathbf{S})_{i,j+\frac{1}{2}}$ can be obtained from Eqs. (38) and (44):

$$\delta(\mathbf{E}\cdot\mathbf{S})_{i,j+\frac{1}{2}} = S_{i,j+\frac{1}{2}}\left(\tilde{\mathbf{A}}_j\delta U_{j-1}+\tilde{\mathbf{B}}_j\delta U_j +\tilde{\mathbf{C}}_j\delta U_{j+1}+\tilde{\mathbf{D}}_j\delta U_{j+2}\right) \quad (58)$$

where

$$\tilde{\mathbf{A}}_j = \frac{1}{2}\left[\mathbf{M}(\mathbf{U^L})+\hat{\mathbf{T}}|\hat{\mathbf{\Lambda}}|\hat{\mathbf{T}}^{-1}\right]\left(-\frac{1}{2}\alpha_4\right) \quad (59)$$

$$\tilde{\mathbf{B}}_j = \frac{1}{2}\left[\mathbf{M}(\mathbf{U^R})-\hat{\mathbf{T}}|\hat{\mathbf{\Lambda}}|\hat{\mathbf{T}}^{-1}\right]\left(\frac{1}{2}\alpha_2\right) + \frac{1}{2}\left[\mathbf{M}(\mathbf{U^L})+\hat{\mathbf{T}}|\hat{\mathbf{\Lambda}}|\hat{\mathbf{T}}^{-1}\right]\left[\mathbf{I}+\frac{1}{2}(\alpha_4-\alpha_3)\right] -\mathbf{B_v}\frac{\partial V}{\partial U} \quad (60)$$

$$\tilde{\mathbf{C}}_j = \frac{1}{2}\left[\mathbf{M}(\mathbf{U^R})-\hat{\mathbf{T}}|\hat{\mathbf{\Lambda}}|\hat{\mathbf{T}}^{-1}\right]\left[\mathbf{I}+\frac{1}{2}(\alpha_1-\alpha_2)\right] + \frac{1}{2}\left[\mathbf{M}(\mathbf{U^L})+\hat{\mathbf{T}}|\hat{\mathbf{\Lambda}}|\hat{\mathbf{T}}^{-1}\right]\left(\frac{1}{2}\alpha_3\right)-\mathbf{A_v}\frac{\partial V}{\partial U} \quad (61)$$

$$\tilde{\mathbf{D}}_j = \frac{1}{2}\left[\mathbf{M}(\mathbf{U^R})-\hat{\mathbf{T}}|\hat{\mathbf{\Lambda}}|\hat{\mathbf{T}}^{-1}\right]\left(-\frac{1}{2}\alpha_1\right) \quad (62)$$

The final global Jacobian matrix for the implicit terms in the semi-implicit Runge-Kuta schemes is a block pentagonal diagonal matrix involving terms along the j grid direction only. The block pentagonal diagonal system of equations can be solved efficiently by numerical methods.

Numerical Results

Code Validation

The semi-implicit Runge-Kutta method is first tested by a steady two-dimensional hypersonic flow over a circular cylinder at Mach 6. The flows conditions are $Re_\infty = 2.50\times10^5$, $p_\infty = 486\,pa$, $T_\infty = 280\,K$, $T_{\text{wall}} = 300\,K$, $\gamma = 1.4$, and cylinder radius is 0.005 meters. The solutions are obtained by marching unsteady Navier-Stokes equations to steady states using the second-order semi-implicit Runge-Kutta scheme. The numerical calculations are performed in a set of 42×142 grids.

Figure 1 shows the comparison of bow shock shape with experimental results by Kim[21]. The results show that the bow shock captured by the second-order semi-implicit TVD scheme agrees well with the experimental data. The pressure contours, which are also shown in the figure, show that the semi-implicit TVD scheme can catch the bow shock front without oscillation. The CFL number used in calculation is only limited by the grid spacing in the tangential direction of the wall, though highly stretched grids are used normal to the wall to resolve the boundary layers. Figure 2 is the comparison of bow shock shape with Hayes' data[22] at Mach number 5. Also the two results agree well with each other.

Unsteady Solutions of a Moving Blunt Wedge

The new semi-implicit scheme for the Navier-Stokes equations is then applied to unsteady hypersonic flow over an oscillating blunt leading edge as shown in Fig. 3. The freestream conditions are

$M_\infty = 8.03$ $\quad p_\infty = 985\,Pa$
$T_\infty = 800\,K$ $\quad T_{\text{wall}} = 1000\,K$
$Re = 2.573\times10^5$ $\quad R_n = 0.0254\,m$

The blunt body oscillates around a fixed point according to the following function:

$$\theta(t) = \theta_{max}\,sin(\omega t) \quad (63)$$

where $\theta_{max} = 12°$ and $\omega = 2\pi\times10^3 s^{-1}$. The corresponding reduced frequency is $k = \frac{\omega r_n}{2U_\infty} = 0.025$.

Figure 4 shows the structured 42×122 computational grids used in numerical calculations. For unsteady calculations, the dynamic grids oscillate with the body as a rigd-body motion. At each time step, the grid speed and its position are determined by the motion of the blunt body. The unsteady computations start from the steady state solution at the initial angle $\theta(t=0) = 0°$.

Figure 5 shows the distribution of wall pressure along the body surface at different moments of the blunt-wedge oscillation. The surface distribution is no longer symmetric about the stagnation line because of the blunt body oscillations. From $t = 2.50\times10^{-4}$ s to $t = 7.48\times10^{-4}$ s, the wall pressure maintains similar shapes but the curves move from left to right. The figure also shows that the highest value of wall pressure is in the regions near the stagnation line. Figure 6 shows the surface heat transfer distribution at the same time stages as that in Fig. 5. Compared with the surface pressure, the surface heating rates are much less affected by the body oscillations. Figure 7 is the viscous stress distributions along the wall. The jump of its value near the shoulder is due to the discontinuous of the surface curvature.

Figure 8 shows the time history of wall pressure

at the stagnation point during the body oscillations. These results show that the oscillation of the stagnation pressure is non-symmetric due to nonlinear effects although the motion of the body has a symmetric line at $\theta = 0$. The time histories of heat transfer and viscous stress at the stagnation point are given in Fig. 9. Again, the non-symmetric characters are inherent for the viscous unsteady flow fields.

Figures 10-12 are the velocity vectors at three time stages. They show that the location of bow shock front changed as the blunt body moving.

Figures 13-22 are pressure contours at ten stages about a oscillation cycle. The flowfield is obviously non-symmetric because the unsteady oscillation.

The magnitude of the maximum time step used in numerical calculation is limited by the stability condition related to the grid size in the streamwise direction. The stiffness of fine grids in the direction across the boundary layers is overcome by the semi-implicit schemes. The computations show that the new schemes are robust with large time steps.

Conclusions

An efficient semi-implicit Runge-Kutta method has been presented for computing unsteady flows around fixed or moving bodies using the unsteady Navier-Stokes equations on structured dynamic grids. The method uses semi-implicit treatment to overcome stiffness in viscous wall-normal derivative terms, while the streamwise terms are computed by explicit methods for efficient unsteady flow calculations. The method has been tested in computations for viscous hypersonic flows over steady and oscillating blunt bodies. Numerical tests show that the semi-implicit method is efficient for solving the Navier-Stokes equations in highly stretched grids across boundary layers. The CFL numbers in the semi-implicit computations are only limited by the streamwise grid spacing and the accuracy requirement for unsteady flow computations.

Acknowledgments

This research was supported by the Air Force Office of Scientific Research under grant numbers F49620-94-1-0019 and F49620-95-1-0405 monitored by Dr. Len Sakell. More information on this work and related ongoing research can be found on the World Wide Web at http://cfdlab5.seas.ucla.edu.

References

[1] D.L. Whitaker. Three-Dimensional Unstructured Grid Euler Computations Using A Full-Implicit,Upwind Method. *AIAA Paper 93-3337CP*, 1993.

[2] D. J. Mavriplis. Three-Dimensional Unstructured Multigrid for the Euler Equations. *AIAA Paper 91-1549CP*, 1991.

[3] S. D. Connell and D. Graham Holmes. A 3D Unstructured Adaptive Multigrid Scheme for the Euler Equations. *AIAA Paper 93-3339CP*, 1993.

[4] T. J. Barth and P. O. Frederickson. Higher Order Solution of the Euler Equations on Unstructured Grids Using Quadratic Reconstruction. *AIAA Paper 90-0013*, 1990.

[5] J. T. Batina. A Fast Implicit Upwind Solution Algorithm for Three-Dimensional Unstructured Dynamic Meshes. *NASA TM-104186*, 1991.

[6] D. L. Whitaker D. C. Slack and R. W. Walters. Time Integration Algorithm for the Two-Dimensional Euler Equations on Unstructured Meshes. *AIAA Journal, Vol.32, pp. 1158-1166*, 1994.

[7] D. G. Holmes and S. D. Connell. Solution of the 2D Navier-Stokes Equations on Unstructured Adaptive Grids. *AIAA Paper 89-1932*, 1989.

[8] S. D. Connell and M. E. Braaten. Semi-Structured Mesh Generation for 3D Navier- Stokes Calculations. *AIAA Paper 95-1679*, 1995.

[9] V. Venkatakrishnan and D. J. Mavriplis. Implicit Method for the Computation of Unsteady Flows on Unstructured Grids. *AIAA Paper 95-1705*, 1995.

[10] D. G. Bishop and R. W. Noack. An Implicit Flow Solver with Upwind Differencing for Three-Dimensional Hybrid Grids. *AIAA Paper 95-1707CP*, 1995.

[11] G. A. Ashford and K. G. Powell. Adaptive Unstructured Triangular Mesh Generation and Flow Solvers for the Navier-Stokes Equations at High Reynolds Number. *AIAA Paper 95-1724CP*, 1995.

[12] M. J. Marchant D. L. Marcum, N. P. Weatherill and F. Beaven. Adaptive Unstructured Grid Generation for Viscous Flow Application. *AIAA Paper 95-1726*, 1995.

[13] M. E. Braaten and S. D. Connell. A 3D Unstructured Adaptive Multigrid Scheme for the Navier-Stokes Equations. *AIAA Paper 95-1728CP*, 1995.

[14] B. K. Soni R. P. Koomullil and C. Huang. Navier-Stokes Simulation on Hybrid Grids. *AIAA Paper 96-0768*, 1996.

[15] M. Soetrisno S. T. Imlay and D. W. Rooberts. Coupled Flow and Heat Transfer Analysis Using Structured-Unstructured Grids. *AIAA Paper 96-0622*, 1996.

[16] Y. Kallinderis A. Khawaja and V. Parthasarathy. Implementation of Adaptive Hybrid Grids for 3-D Turbulent Flows. *AIAA Paper 96-0026*, 1996.

[17] L. Kleiser and T.A. Zang. Numerical Simulation of Transition in Wall-Bounded Shear Flows. *Annual Review of Fluid Mechanics*, Vol. 23, pp. 495-535, 1991.

[18] X. Zhong. Additive Semi-Implicit Runge-Kutta Methods for Computing High-Speed Nonequilibrium Reactive Flows. *AIAA Paper 95-2077*, 1995.

[19] J. W. Shen and X. Zhong. Semi-Implicit Runge Kutta Schemes for Non-Autonomous Differentia Equations in Reactive Flow Computations. *AIA. Paper 96-1969*, 1996.

[20] P. L. Roe. Characteristic Based Scheme for th Euler Equations. *Annual Review of Fluid Mechar ics*, Vol.18, pp. 337-365, 1986.

[21] C. Kim. Experimental Studies of Supersonic Flo Past a Circular Cylinder. *Journal of the Physic Society of Japan*, Vol. 11, No. 4, 1956.

[22] Wallace D. Hayes and Ronald F. Probstein. Hy personic Flow Theory. *Academic Press Inc.*, 195

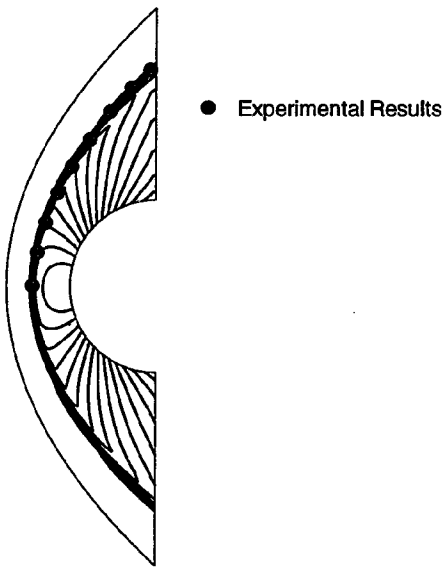

Figure 1: Comparison of the bow shock shape with experimental data by Kim (1956) for Mach 6 flow over a cylinder.

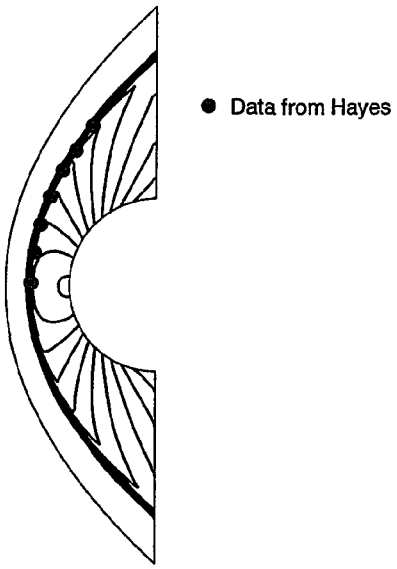

Figure 2: Comparison of the bow shock shape with Hayes' data for Mach 5 flow over a cylinder.

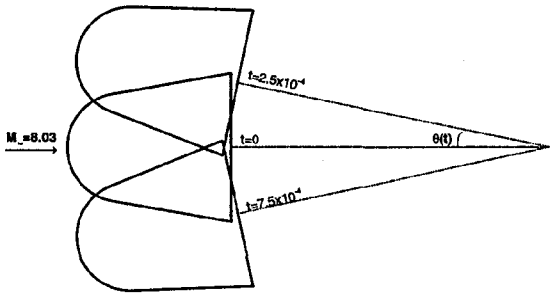

Figure 3: Schematics of Mach 8.03 flow over an oscillating blunt leading edge at three different moments in time.

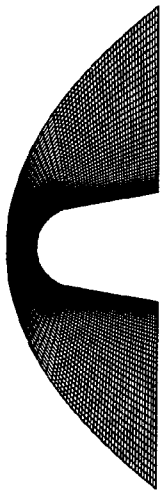

Figure 4: Computational grids in hypersonic flow over the oscillating body.

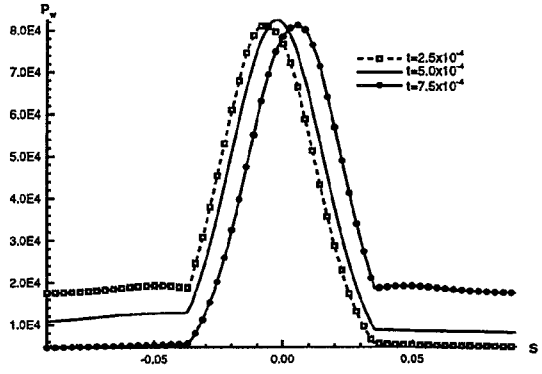

Figure 5: Distributions of pressure along the body surface at three moments during the oscillations.

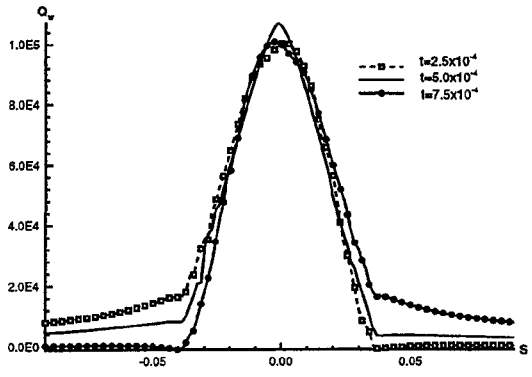

Figure 6: Distributions of surface heating rate along the body surface at three moments during the oscillations.

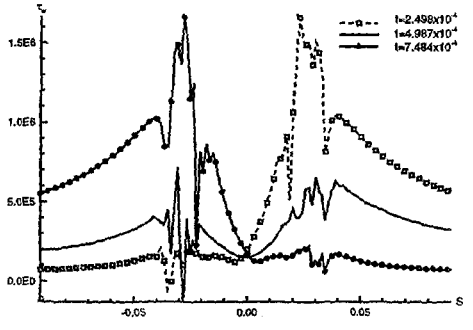

Figure 7: Distributions of viscous stress along the body surface at three moments during the oscillations.

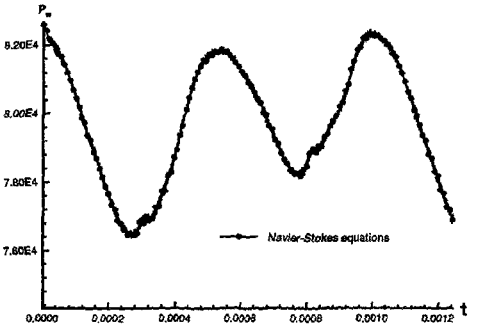

Figure 8: Time history of the pressure at the stagnation point.

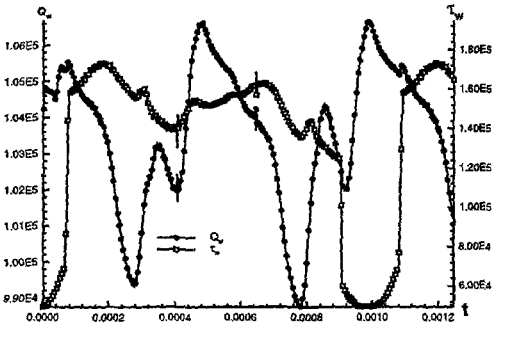

Figure 9: Time history of the heat transfer rate and viscous stress at the stagnation point.

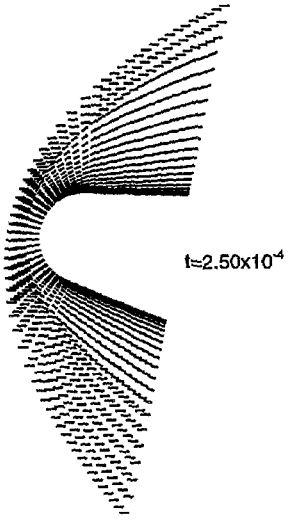

Figure 10: The velocity vectors at three successive moments of the time during the body oscillations, $t=2.50\times10^{-4}$.

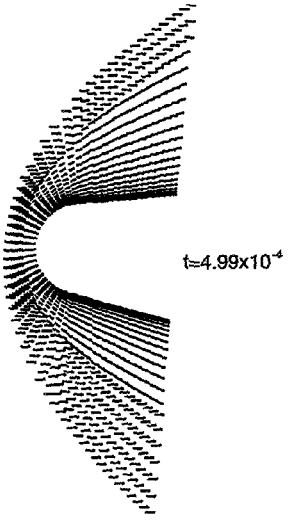

Figure 11: The velocity vectors at three successive moments of the time during the body oscillations, $t=4.99\times10^{-4}$.

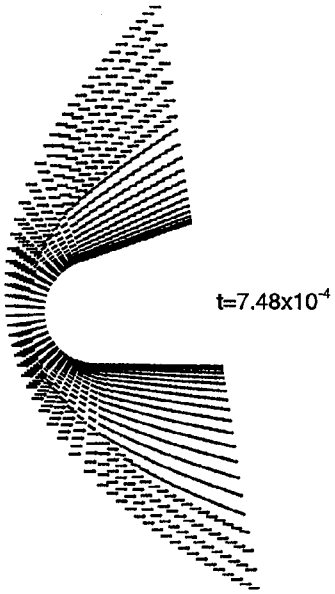

Figure 12: The velocity vectors at three successive moments of the time during the body oscillations, t=7.48×10^{-4}.

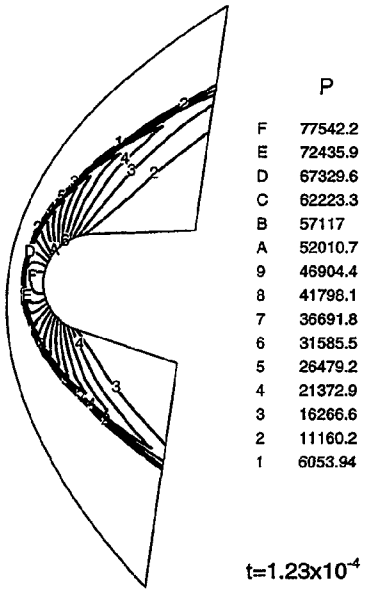

Figure 14: The instantaneous pressure contours at ten successive moments of the time during the body oscillations.

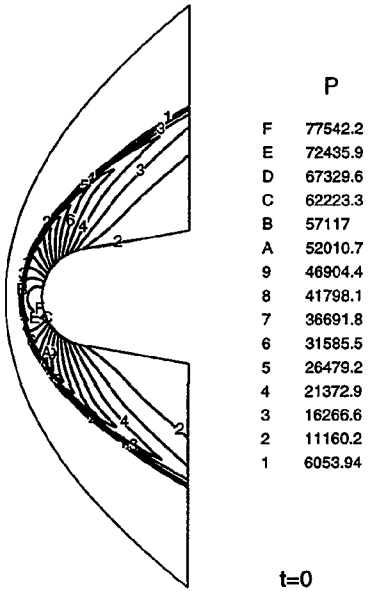

Figure 13: The instantaneous pressure contours at ten successive moments of the time during the body oscillations.

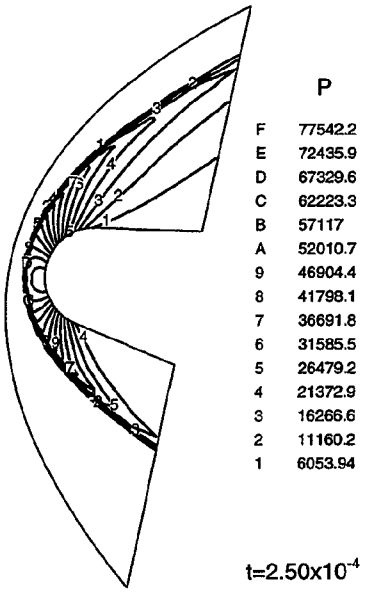

Figure 15: The instantaneous pressure contours at ten successive moments of the time during the body oscillations.

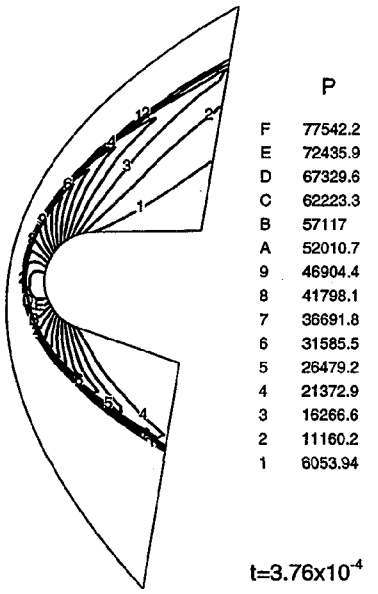

Figure 16: The instantaneous pressure contours at ten successive moments of the time during the body oscillations.

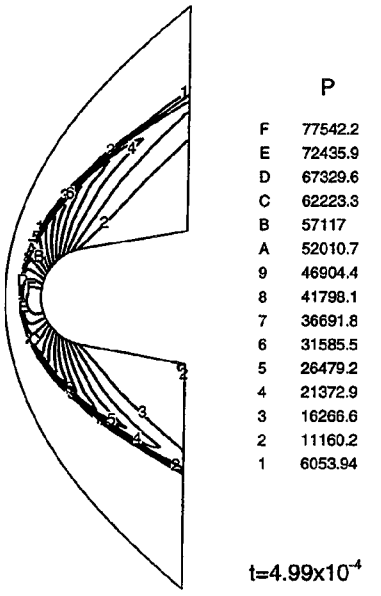

Figure 17: The instantaneous pressure contours at ten successive moments of the time during the body oscillations.

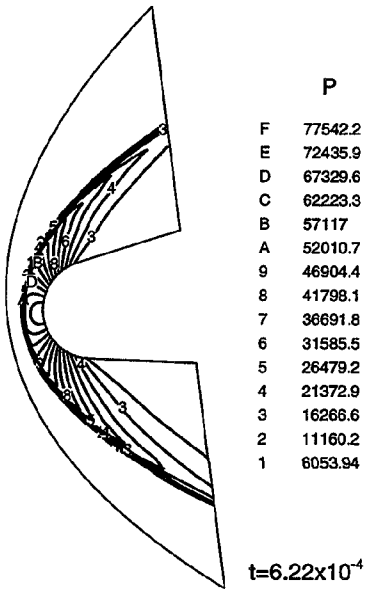

Figure 18: The instantaneous pressure contours at ten successive moments of the time during the body oscillations.

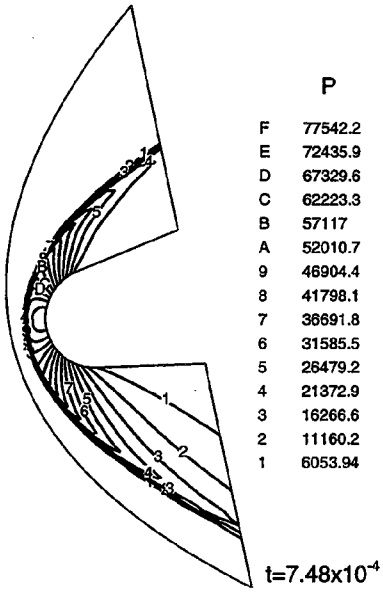

Figure 19: The instantaneous pressure contours at ten successive moments of the time during the body oscillations.

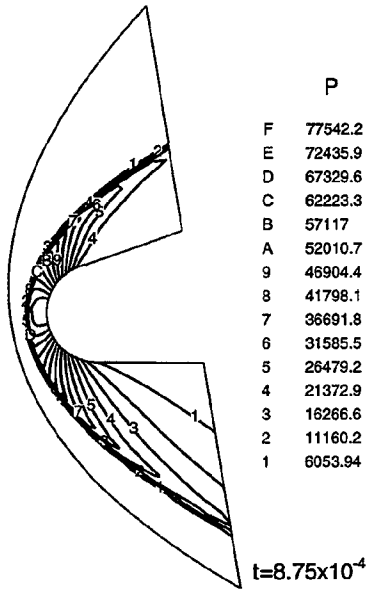

Figure 20: The instantaneous pressure contours at ten successive moments of the time during the body oscillations.

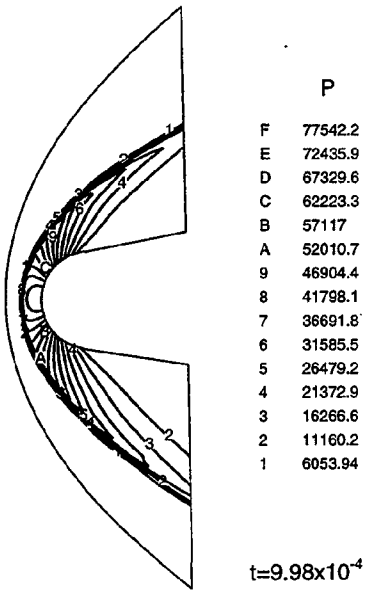

Figure 21: The instantaneous pressure contours at ten successive moments of the time during the body oscillations.

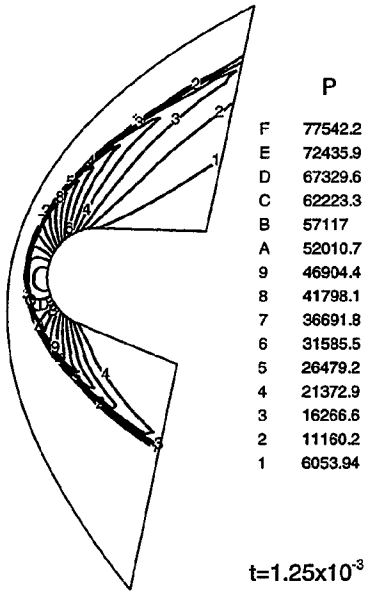

Figure 22: The instantaneous pressure contours at ten successive moments of the time during the body oscillations.